Eliminating Current Sensor Dependencies in DAB Converters using a Luenberger Observer-based Hybrid Approach

Piyali Pal, *Graduate Student Member, IEEE,* Ranjan Kumar Behera, *Senior Member, IEEE,* and Utkal Ranjan Muduli, *Senior Member, IEEE*

***Abstract*—A robust and sensorless control strategy is presented for dual active bridge (DAB) converters for electric vehicle (EV) charging application. In this paper, the Luenberger Observer-based sliding mode control has been developed. The observer successfully estimated the load current, retaining the benefits of sliding-mode control. Moreover, the observer has been modified to suppress the double-line frequency ripple at the output of the DAB converter when integrated with a single-phase AC-DC converter. This paper delves into a detailed mathematical modeling of DAB converters utilizing reduced-order models to minimize computational complexity. The modeling is accompanied by a detailed stability analysis. This paper provides comprehensive guidelines for controller design and parameter selection. To validate the proposed theoretical framework, a hardware prototype was developed in the laboratory, which was subjected to various experimental scenarios, including load variations, parametric changes, and cascade architecture. The experimental results confirm the effectiveness and robustness of the proposed control strategy.**

***Index Terms*—EV Charging Infrastructure; Dual Active Bridge Converter; Sliding Mode Control; Luenberger Observer; Sensorless Control.**

NOMENCLATURE

DAB	Dual Active Bridge.
ESS	Energy Storage System.
LO	Luenberger Observer.
NDO	Nonlinear Disturbance Observer.
SMC	Sliding Mode Control.
SPS	Single Phase Shift.
SST	Solid State Transformer.
STSMC	Super Twisting Sliding Mode Control.
V_i	Input DC-link supply.
v_o	Output voltage of the converter.
v_p,v_s	Primary and secondary voltage of the transformer.
i_p, i_i	Current through the leakage inductor, input current, respectively.
L_p	Effective leakage inductance.
i_o, i_c, i_L	Output current, current through C_o, load current, respectively.
f_{sw}	Switching frequency.
φ	Phase shifting angle.
P_t	Transmitted power.
d	Phase shift ratio.
ρ	Sliding surface.
V_o^*	Reference output voltage.
κ_1, κ_2	Sliding-mode gains.
i_o^*	Reference output current.
V_L	Lyapunov function for sliding mode control
l_1,l_2	Observer gains.
g_n(s)	Transfer function of the notch filter.
J_L	Lyapunov function for the Luenberger observer.
ζ, g_{min}	Damping factor and gain at the cutoff frequency of the notch filter.

Manuscript received on Dec, 27, 2023, revised Mar, 19, 2024, Accepted Mar, 27, 2024.

This work is supported by the research grant by NIDHI-PRAYAS scheme of the NSTEDB, DST, Incubation Centre IIT Patna. *(Corresponding Authors: Piyali Pal and Utkal Ranjan Muduli)*

Piyali Pal and Ranjan Kumar Behera are with the Dept. of Electrical Engineering, Indian Institute of Technology Patna, Bihta, 801103, India. (e-mail: piyali_2021ee24@iitp.ac.in; rkb@iitp.ac.in)

Utkal Ranjan Muduli is with APEC, EECS Dept., Khalifa University, Abu Dhabi, 127788, United Arab Emirates. (e-mail: utkal.muduli@ku.ac.ae)

I. INTRODUCTION

Dual Active Bridge (DAB) converters are crucial in DC microgrids. DAB can act as a link between energy storage systems (ESSs) and the DC microgrid, enabling energy exchange between them with electrical isolation. Solid-state transformers (SSTs) based on DAB have been implemented in power grids to connect various scales of microgrids or various levels of DC grids. The use of DAB may lighten weight and increase energy efficiency [1], [2]. When grid-to-vehicle capability is necessary, DAB is also a viable option to charge batteries onboard in plug-in electric cars [3]. The DAB converter has stimulated the power electronics sector due to its many advantages such as galvanic isolation, bidirectional power flow, flexibility in voltage conversion, inherent soft switching, high efficiency, etc. These applications are prone to various disturbances, such as frequent changes in load and variations in input side voltage. Therefore, robust control with a fast dynamic response is an inevitable requirement because a large deviation in output voltage response may lead the system to an unstable state.

Modeling the DAB converter poses unique challenges due to the high-frequency AC nature of the inductor current with zero average value. The accuracy of the controller design and its performance depend on the chosen modeling approach, which requires a precise small signal model for the converter. The generalized average model of DAB is proposed in [4], where the current dynamics of the inductor is considered for

the controller design. On the contrary, the discrete-time model presented in [5] offers high accuracy and enhanced control for digital implementations; however, it requires specialized tools due to its computational complexity. Alternatively, the reduced-order model introduced in [6], simplifies the closed-loop system by ignoring the high-frequency inductor current dynamic. Closed-loop output voltage feedback control is a common technique for regulating the output voltage of DAB [7]. However, the DAB converter is non-linear in nature in relation to the operating point of the load power. To maintain optimum dynamic performance, it is important to modify the controller gain according to the load for every control action. Moreover, traditional linear control techniques for the DAB converter reported in the literature are fixed gain PI control loop [8], feedback linearization control [9], etc. However, the performance of the above-mentioned controllers significantly deteriorates under load variation. A linear controller operates under extremely narrow bandwidth.

To enhance robustness during load disturbance, a load current feed-forward controller has been implemented in [10]–[12]. In [10], the feedforward gains are selected from a predefined look-up table according to the variation of the load. The load current is used as a feedback signal in the control loop of the model-based phase shift control proposed in [11]. But here the feedforward gain is calculated online, which increases the complexity of the system, and also these controllers are parameter sensitive. In [12] virtual direct power-based control has been proposed, which measures the output power of the converter and uses it as a feedforward signal in the control loop. It eliminates the dependency on using the exact value of the leakage inductance, but it shows poor dynamic performance under light load conditions. In [13] disturbance observer-based control of the DAB converter has been implemented. This control technique employed an observer who could estimate the total disturbance of the system without using additional sensors. It showed superior performance in disturbance rejection, but increased computational complexity. Predictive control of the output voltage has been reported in [14]. It has the distinguishing characteristic of fast dynamic performance, but requires detailed information about the plant and a proper selection of weighted factors. Inappropriate control parameters can cause system instability. In [15] the predictive current control method for the DAB converter has been proposed, but this controller is not feasible for high-frequency applications. A fuzzy controller in [16] can be a reliable solution to achieve a fast dynamic response without knowing much about accurate plant modeling and information about the system parameters. But stability analysis is challenging and controller design is quite complex. Due to its simplicity of construction, robustness against external disturbances, and ease of implementation, sliding-mode control has generated a lot of interest in nonlinear control. However, traditional sliding-mode control has two major drawbacks. One is the chattering problem, and the other is sensitivity to unmodeled disturbances, widely known as mismatched disturbances. A double integral sliding mode control for the regulation of voltage and current of the dual active bridge converter has been presented in [17]. It has reduced the chattering problem to some extent, but harmonic model-based control has been utilized there, which increases computational complexity. In [18] super-twisting sliding mode control (STSMC) of the DAB converter has been reported. STSMC control minimizes the chattering effect and shows robustness against parameter variation. However, proper care should be taken to determine the values of α, and β. To address the chattering issue while preserving its nominal control performance, numerous authors in [19], [20] proposed disturbance observer-based sliding mode control. The objective is to construct an equivalent control law in which the disturbance is estimated and used as a feedforward compensation. Moreover, observer-based sliding mode control has also been used for sensorless fault-tolerant control of power electronics converters. Existing research on fault-tolerant techniques in power electronic converters offers a variety of approaches to address power semiconductor device failures [21]. Decentralized strategies are crucial in large-scale systems, particularly when handling coupled sensor and actuator faults [22]. Higher-order sliding-mode observers (SMOs) provide finite-time convergence of system response and reduced chatter, enhancing fault tolerance in applications such as DC servomotors [23]. Adaptive versions of SMOs further improve performance in dynamic environments [24]. In particular, SMOs can be used to reconstruct phase current errors and estimate the position of the rotor, allowing fault-tolerant control (FTC) without dedicated current sensors [25]. Quasi-Luenberger observers combined with robust sliding mode controllers mitigate disturbances in power converter dynamics [26]. The use of higher-order SMOs can also optimize power extraction in DC-DC converters used for photovoltaic energy applications [27]. Sensorless control employing a load current estimator has been presented in [19], [20] has suggested first-order load current observer-based control for DC-DC boost converters. But the predicted error was rather substantial since the observer's model had shortcomings and additional parasitic effects were present. To estimate the output disturbance, a model-predictive control approach has been used. However, the procedure is lengthy and includes complicated calculations. To estimate the load current disturbance and the input voltage variation in the DC-DC boost converter, a non-linear disturbance observer (NDO) has been proposed. NDO demonstrates a superior estimate. In [28], [29] A three-phase grid-tied inverter DC-link current has been estimated using a non-linear disturbance observer and the Luenberger observer.

In the earlier version of this article, cited as [1], the concept of a current sensorless observer-based sliding mode control for the DAB converter was introduced. However, stability analysis, the design of observer parameters, and real-time validation remained unaddressed. Moreover, a pronounced double-line frequency ripple in the output voltage was observed during hardware implementation when the Dual Active Bridge (DAB) was coupled with an AC/DC converter. To alleviate this ripple, modifications were subsequently made to the proposed observer. Therefore, this work offers a proposal for the current sensorless sliding mode control of Dual Active Bridge converters. The load current is calculated using the Luenberger observer. This paper outlines the following significant

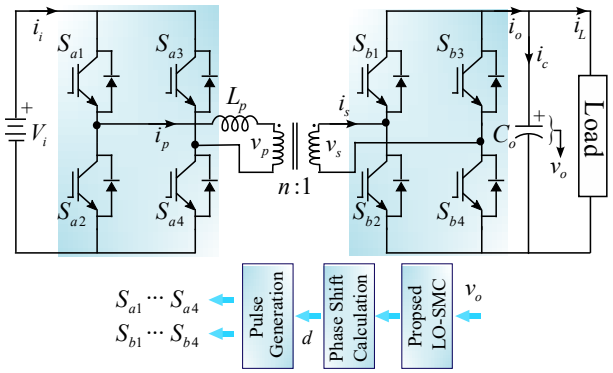

Fig. 1. DAB converter topology with proposed control.

contributions.

- A reduced-order model of the DAB converter has been employed for a simplified approach to SMO design. This contrasts with traditional, more complex controller designs and could lead to potential benefits in computational efficiency.
- Accurate load current estimation and mitigation of double-line frequency ripple have been achieved through a tailored LO design. This combined functionality is especially advantageous in the context of cascaded DAB converters with rectifiers.
- The stability of the proposed controller has been extensively analyzed using the Lyapunov stability theory, providing a strong theoretical basis for its robustness. Additionally, its resilience has been demonstrated through rigorous testing under both parametric variations and load disturbances. This shows its potential for reliable performance in practical applications.

This paper is structured as follows: Section II outlines the working principle and modeling of the system. Section III delves into the controller's design, selection of parameters for the controller, and theoretical analysis of stability and robustness. In Section IV, the experimental results for a prototype DAB converter are provided, along with a comparison of its performance against traditional controllers. Section V concludes this article on the basis of the results of the experiment.

II. Operation of DAB converter

A. Circuit configuration

Fig. 1 shows the circuit configuration of the DAB converter. It consists of two active bridges (a and b) connected to the primary and secondary sides of the isolated high-frequency transformer (with turn ratio $n:1$), respectively. $S_{a1},\ldots,S_{a4}$ and $S_{b1},\ldots,S_{b4}$ are active switches on the bridges a and b. The input DC-link supply voltage to the primary side bridge a is V_i, while v_o is considered the output DC-link voltage. v_p and v_s are the voltages in the primary and secondary windings of the transformer; i_p is the current through the effective leakage inductance on the primary side of the transformer L_p, while i_i is the input current drawn from the DC source. Similarly, i_o is the output current of the bridge b, which is divided further into the current through the capacitor C_o, i.e., i_c and the load current i_L.

The phase change between the two bridges controls the converter power flow. If the bridge a has a leading phase, then the power will flow from a to b and vice versa. In this paper, the single-phase shift (SPS) modulation technique is adopted to control power flow. A typical characteristic timing diagram of the single-phase shift modulation technique is shown in Fig. 2(a). Both bridges generate square waves with a duty ratio of 50% at a fixed switching frequency f_{sw}. But the voltage v_s is lagging behind v_p due to a phase shift angle φ that is responsible for the power flow between two bridges.

B. Reduced order modeling of DAB

Modeling of a DAB converter seems more difficult than a conventional DC-DC converter due to the presence of the leakage inductor current i_p, which is pure AC. In this paper, a reduced-order model of the DAB converter is carried out. Therefore, the dynamics of i_p is neglected. The dynamic response of i_p does not affect the disturbance of the phase change or the change in output voltage. This is due to the isolation transformer, and the dynamics of the output voltage is much slower than the dynamics of the inductor current. The power transmitted (P_t) from the bridge a to b can be represented as (1).

$$P_t = \frac{nV_i v_o}{2f_{sw}L_p} d(1-d), \quad -0.5 < d < 0.5 \tag{1}$$

where d is the phase shift ratio and can be defined as $d = \varphi/\pi$. If no loss is considered in the system including conduction loss and switching loss, then by equating the input and output power with the delivered power, the expression of the input current i_i and the output current i_o can be calculated.

$$\begin{aligned} i_i &= \frac{nv_o}{2f_{sw}L_p} d(1-d), \quad -0.5 < d < 0.5 \\ i_o &= \frac{nV_i}{2f_{sw}L_p} d(1-d), \quad -0.5 < d < 0.5 \end{aligned} \tag{2}$$

The value of d can be derived from (2) for both directions of the power flow, which is mentioned in Section III-A. The physical existence of d can be appropriately visualized from Fig. 2(a), which can be obtained from the controller diagram mentioned in Fig. 2(b).

III. Proposed LO-SMC Methodology

This section focuses on the design of a sliding mode controller (SMC) for a DAB converter, in order to improve the system modeling and reduce chattering. To enhance stability, a continuous function replaces the discontinuous signum function traditionally used in SMC. The sliding surface, crucial for control, is defined with constants κ_1 and κ_2. These constants help ensure both the stability and convergence of dynamic errors. Fig. 2(b) illustrates the block diagram of the LO-SMC design, where the output voltage of the converter is measured directly. This measured voltage is used by both the observer (which estimates the load current) and the sliding-mode controller. The controller generates control law to regulate the

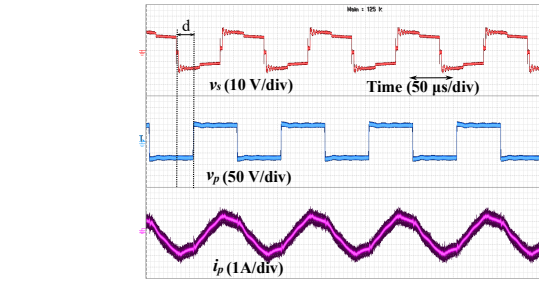

(a)

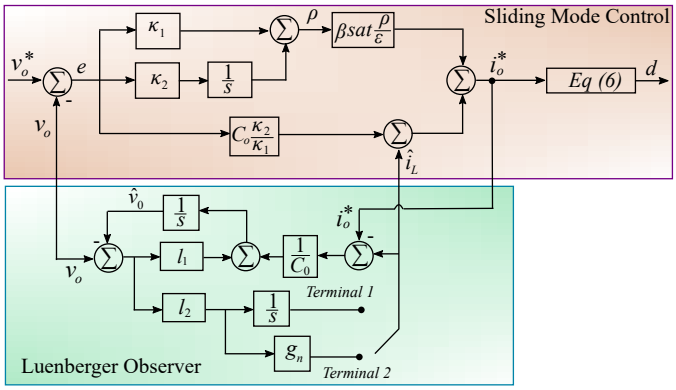

(b)

Fig. 2. (a) Timing waveform under single phase shift (SPS) modulation and (b) proposed control strategy.

output voltage, while the observer block estimate the load current and offers flexibility for different system configurations (fixed DC link or cascaded DAB-AC/DC converter).

A. Design of the sliding mode control

In the design of a non-linear SM-based control for the DAB converter, two key factors are considered. First, system modeling involves accounting for voltage, current, and circuit parameters. Second, addressing chattering issues is crucial. The SM controller typically employs a signum function to maintain state variables on the sliding surface, but its discontinuous nature causes high-frequency ripples in the control variable, leading to chattering. To overcome this, the paper adopted a continuous or smooth function, such as a saturation function instead of the discontinuous sgn function. This approach is used to regulate the output voltage and design the SMC, where the sliding surface ρ is specifically defined for effective control as $\rho = \kappa_1 e + \kappa_2 \int e\ dt$.

$$\dot{\rho} = \kappa_2 e + \kappa_1 \dot{e} = \kappa_2 e + \kappa_1(-\dot{v}_o) \tag{3}$$

where e (=$V_o^* - v_o$) represents the error voltage between the reference output voltage V_o^* and v_o. κ_1, κ_2 are the positive constants that ensure the stability and convergence rate of the error dynamics. The dynamics of the output voltage ($\dot{v}_o$) for the system shown in Fig. 1, can be expressed as $\dot{v}_o = C_o^{-1}(i_o - i_L)$. To derive the control law, the derivative of the sliding surface is equal to zero. Therefore, we can write

$$\dot{\rho} = \kappa_2 e + \frac{\kappa_1}{C_o}(i_L - i_o) \quad \Rightarrow i_o|_{\dot{\rho}=0} = \frac{\kappa_2 C_0}{\kappa_1} e + i_L \tag{4}$$

Now, the equivalent control law can be defined as (5) to obtain the estimated reference output current i_o^*.

$$i_o^* = \frac{\kappa_2 C_0}{\kappa_1} e + i_L + \beta sat\left(\frac{\rho}{\varepsilon}\right) \tag{5}$$

where ε is a positive constant and β is the controller gain that has to be chosen such that the system trajectory fulfills the reachability condition. The function $sat(\frac{\rho}{\varepsilon})$ can be denoted as $\frac{\rho}{\varepsilon}$, if $|\rho| \le |\varepsilon|$, $+1$, if $\rho > \varepsilon$, and -1, if $\rho < \varepsilon$. After generating the equivalent control signal, it can be transformed to the required phase shift ratio d by solving (2) and replacing $i_o = i_o^*$.

$$d = \begin{cases} \frac{1}{2} - \sqrt{\frac{1}{4} - \frac{2f_{sw}L_p}{nV_i} i_o^*}, & \text{for } i_o^* \ge 0 \\ -\frac{1}{2} + \sqrt{\frac{1}{4} + \frac{2f_{sw}L_p}{nV_i} i_o^*}, & \text{for } i_o^* \le 0 \end{cases} \tag{6}$$

The only information in (5), which is not available in practice is the term i_L. This signal can be estimated using the Luenberger Observer. The designed procedure is explained in Section III-B. With the estimated signal, the control law (5), can be rewritten as

$$i_o^* = \frac{\kappa_2 C_0}{\kappa_1} e + \hat{\chi}_2 + \beta sat\left(\frac{\rho}{\varepsilon}\right) \tag{7}$$

where $\hat{\chi}_2$ is the estimated load current. Proper selection of controller parameters is an essential practice [18]. Here, κ_1 and κ_2 must be determined so that the state vector converges quickly to zero steady-state error. The motion of the sliding manifold at $\rho = 0$ is $\kappa_1 e + \kappa_2 \int e\, dt = 0$. By solving this, the error dynamics, represented by $e = \kappa_0 e^{(-\kappa_2/\kappa_1)t}$, will asymptotically approach zero over time for positive values of κ_1 and κ_2.

$$\kappa_0 e^{(-\kappa_2/\kappa_1)t} \le 0.05 v_o \quad \text{and} \quad \frac{\kappa_2}{\kappa_1} > \frac{\ln 20}{t}. \tag{8}$$

Furthermore, by ensuring that the output voltage error stays below 5%, the coefficients κ_0, κ_1, and κ_2 can be appropriately estimated from (8).

1) Stability Analysis of SM Controller: Prior to stability analysis, it is assumed that a control law i_o^* closely follows the current i_o. Because ε is a positive quantity and $\beta >0$ has taken. Therefore, the trajectory of the system reaches the boundary layer $|\rho| \le |\varepsilon|$ in finite time. When the trajectory of the system reaches the boundary layer, the output DC link voltage converges to its reference voltage based on κ_1 and κ_2 and then the control input i_o^* will follow the i_o. The basic concept of stability analysis is that the motion of any system is always stable if the total energy of a system is always decreasing. The Lyapunov function (V_L) is defined as $V_L = \rho^2/2$ [18]. To ensure stability of the sliding surface and the state trajectory, it must meet the reachability condition, which is that the time derivative of the Lyapunov function must be negative when $\rho \ne 0$, i.e., $\dot{V}_L(\rho) = \rho\dot{\rho} < 0$. Here, ρ and $\dot{\rho}$ can be taken from (3). Replace i_o with an equivalent control law in (5)

$$\dot{\rho} = \kappa_2 e + \frac{\kappa_1}{C_o}\left[i_L - \frac{\kappa_2 C_o}{\kappa_1} e - i_L - \beta sat\left(\frac{\rho}{\varepsilon}\right)\right] \tag{9}$$

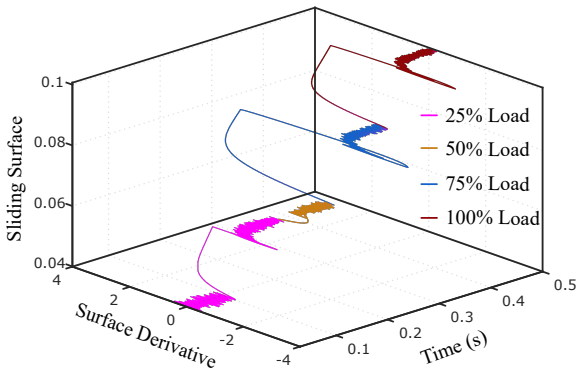

Fig. 3. Trajectory of sliding surface at 25%, 50%, 75%, 100% load.

Substituting (9) in , the time derivative of the Lyapunov function is negative.

$$\dot{V}_L(\rho) = \rho\dot{\rho} = \rho\left(-\beta sat\left(\frac{\rho}{\varepsilon}\right)\right) < 0 \tag{10}$$

Fig. 3 shows the trajectory of the sliding surface when the load is increased by 25%, 50%, 75% and 100% at time $t = 0.1$ s, $t = 0.2$ s, $t = 0.3$ s, $t = 0.4$ s. It depicts the transient response of the sliding surface and its derivative with respect to time. It can be seen that the surface derivative reaches zero within 5 ms after disturbances, which implies that the state vector remains on the sliding surface and approaches the reference vector. Also, it can be inferred from the trajectory plot that the chattering phenomenon is sufficiently reduced by incorporating boundary layer sliding mode control.

B. Designing of the observer

To design the observer, the output voltage v_o and the load current i_L are considered as state vectors, i.e., $\{v_o, i_L\} \rightarrow \{\chi_1, \chi_2\}$. The dynamical model of the system can be obtained in terms of χ

$$\dot{\chi}_1 = \frac{1}{C_0}(i_o - \chi_2), \quad \dot{\chi}_2 = f(\chi, t), \quad y_\chi = \chi_1 \tag{11}$$

The dynamic expression of the load current is considered here as a function of two state vectors χ_1 and χ_2 and y_χ is the sensed output voltage of the converter. For the sake of simplicity in estimator design, it is assumed that the load current is in steady state, which implies that the term $f(\chi, t)$ is equal to zero and the assumption of $\lim_{t\to\infty} \dot{i}_L = 0$ becomes reasonable for DC systems. By rearranging (11) in the state-space model given below,

$$\dot{\chi} = \mathrm{A}\chi + \mathrm{B}u, \qquad y_\chi = C\chi \tag{12}$$

where, $\chi = [\chi_1\ \chi_2]^T$, $A = [0\ -1/C_o; 0\ 0]$, $u = i_o$, $B = [1/C_o;\ 0]^T$, $C = [1\ 0]$. Here, i_o is the control input obtained from the sliding-mode control. Therefore, i_o can be replaced by i_o^*. Now, the Luenberger observer can be designed as follows.

$$\begin{bmatrix} \dot{\hat{\chi}}_1 \\ \dot{\hat{\chi}}_2 \end{bmatrix} = \begin{bmatrix} 0 & -\frac{1}{C_o} \\ 0 & 0 \end{bmatrix} \begin{bmatrix} \hat{\chi}_1 \\ \hat{\chi}_2 \end{bmatrix} + \begin{bmatrix} \frac{1}{C_o} \\ 0 \end{bmatrix} i_o^* + \begin{bmatrix} l_1 \\ l_2 \end{bmatrix} (y_\chi - \hat{y}_\chi) \tag{13}$$

$$\hat{y}_\chi = C\hat{\chi} \tag{14}$$

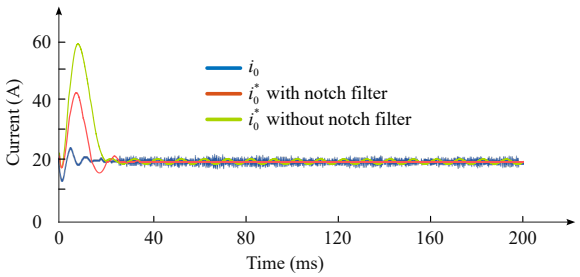

Fig. 4. Control law of sliding mode control without and with notch filter.

where $(\hat{.})$ denotes the estimated states and l_1 and l_2 are the observer gain. The convergence rate of the system and its stability are determined by the values of the observer gain. In typical medium-voltage battery charging applications, where a DAB converter is cascaded with a single-phase AC/DC converter, double-line frequency ripple becomes a significant issue. This ripple can negatively affect battery life and reduce efficiency [30]. Several approaches have been explored to mitigate double-line frequency ripple, including: 1) Proportional integrated resonant controllers (limited in phase margin and system dynamics considerations) [7], 2) Reducing output impedance of DAB converters [31], 3) Disturbance observer-based control (requires crucial stability analysis) [32], and 4) Active power circuits for pulsating power decoupling (increases cost, size, and complexity) [33]. Our specific focus lies in suppressing double-line frequency ripple using a carefully designed observer with notch filters. To achieve this, the observer proposed in (13) needs to be modified to (15). Hence, this LO-SMC approach has the potential advantage of maintaining the overall dynamics of the system.

$$\begin{bmatrix} \dot{\hat{\chi}}_1 \\ \dot{\hat{\chi}}_2 \end{bmatrix} = \begin{bmatrix} 0 & -\frac{1}{C_o} \\ 0 & 0 \end{bmatrix} \begin{bmatrix} \hat{\chi}_1 \\ \hat{\chi}_2 \end{bmatrix} + \begin{bmatrix} \frac{1}{C_o} \\ 0 \end{bmatrix} i_o^* + \begin{bmatrix} l_1 \\ g_{ns} l_2 \end{bmatrix} (y_\chi - \hat{y}_\chi) \tag{15}$$

An integrator $(1/s)$ in the observer loop is sufficient to achieve a zero steady state error, but is not sufficient to suppress the frequency ripple (2ω). Therefore, a notch filter is used in the current observer loop. Here, g_{ns} is the time domain function of $s.g_n(s)$ with $g_n(s)$ as the transfer function of the notch filter.

$$g_n(s) = \frac{s^2 + 2g_{\min}\zeta\omega_{2n}s + {\omega_{2n}}^2}{s^2 + 2\zeta\omega_{2n}s + {\omega_{2n}}^2} \tag{16}$$

where g_{min} is the gain at notch frequency, ζ is the attenuation factor or damping ratio and ω_{2n} is the tuning frequency of the filter which is the double line frequency in our control. As illustrated in Fig. 4, the implementation of the notch filter demonstrably reduces the ripple in the control law compared to the scenario without filtering.

Since the control law directly influences the switching pattern of the converter, a less rippled control law translates to a reduction of the ripple in the output voltage. Substituting the value of $\hat{y}_\chi$ of (14) into (13)

$$\dot{\hat{\chi}} = (A - LC)\hat{\chi} + Bu + Ly_\chi, \quad \hat{y}_\chi = C\hat{\chi} \tag{17}$$

From Fig. 2(b) the simplified current loop of the proposed observer can be derived and is shown in Fig. 5. The transfer

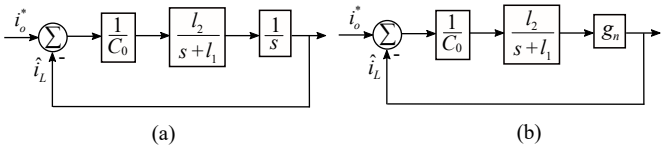

Fig. 5. Current observer loop (a) without and (b) with notch filter.

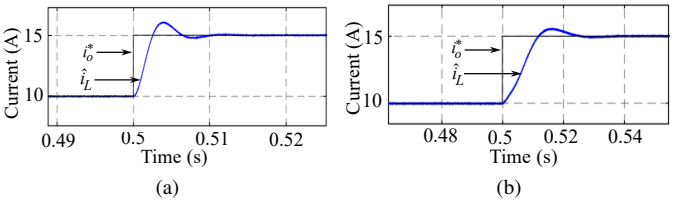

Fig. 6. Transient response of $\hat{i}_L$ (a) without and (b) with notch filter.

function of estimated current to actual current for both cases has been derived in (18) and (19).

$$G_e{}^{LO}(s) = \frac{\hat{\chi}_2}{\chi_2} = \frac{l_2}{s^2 C_0 + s C_o l_1 + l_2} \tag{18}$$

$$G_e^{NF-LO}(s) = \frac{\hat{\chi}_2}{\chi_2} = \frac{g_n l_2}{s C_0 + g_n l_2 + C_o l_1} \tag{19}$$

The observer gain should be chosen such that all the eigenvalues of $(A - LC)$ matrix must have a negative real part. In other words, the choice of L matrix would be made so that the poles of $G_e{}^{LO}(s)$ and $G_e^{NF-LO}(s)$ are sufficiently distant from the imaginary axis towards the left. As a result, the observer quickly converges and the micro-controller estimation loop goes through fewer iterations. The state estimation error progressively approaches zero, as shown in Fig. 6. Figs.7 and 8 show the pole-zero plot of the transfer function derived in $G_e{}^{LO}(s)$ and $G_e^{NF-LO}(s)$ to vary the gain l_1 and l_2 separately. It can be seen that the negative values of l_1 and l_2 shifted the poles on the right-hand side of the imaginary axis, causing instability. Moreover, lower values of l_1 show a longer settling time and too much higher values can cause the system to be overdamped. Whereas higher values of l_2 show faster convergence but higher overshoot.

1) Stability Analysis of Observer: The state estimation error is represented as $\tilde{\chi}_1 = \chi_1 - \hat{\chi}_1$ and $\tilde{\chi}_2 = \chi_2 - \hat{\chi}_2$. Using equations (11) and (13), the time derivative of the estimation error can be expressed as,

$$\dot{\tilde{\chi}}_1 = \frac{1}{C_o} i_o - \frac{1}{C_o}\chi_2 + \frac{1}{C_o}\hat{\chi}_2 - \frac{1}{C_o} i_o - l_1(\chi_1 - \hat{\chi}_1) \tag{20}$$

After simplifying (20), we get $\dot{\tilde{\chi}}_1 = -C_o^{-1}\tilde{\chi}_2 - l_1\tilde{\chi}_1$. Similarly, the error dynamic of $\hat{\chi}_2$ can be written as $\dot{\tilde{\chi}}_2 = -l_2\tilde{\chi}_2$. Now, To check the stability of the designed observer, consider the Lyapunov function as

$$J_L = \frac{1}{2}(\tilde{\chi}_1^2 + \tilde{\chi}_2^2) \tag{21}$$

The system will be stable if the time derivative of the Lyapunov candidate is negative. Therefore, taking the derivative of (21) and substituting the values of $\dot{\tilde{\chi}}_1$ and $\dot{\tilde{\chi}}_2$, the dynamics

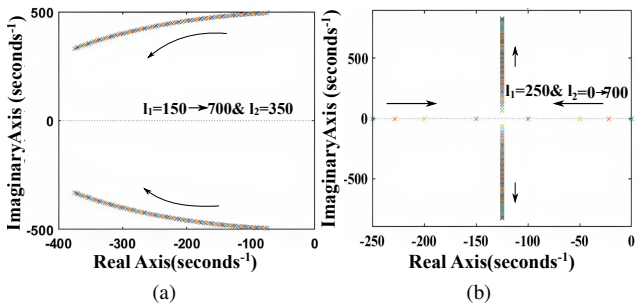

Fig. 7. Close loop poles trajectory of the transfer function $G_e{}^{LO}(s)$, (a) $l_1 : 150 \rightarrow 700$, $l_2 : 350$ (b) $l_2 : 0 \rightarrow 700$, $l_1 : 250$

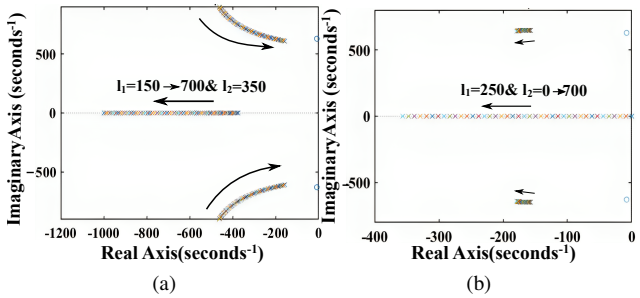

Fig. 8. Close loop poles trajectory of the transfer function $G_e^{NF-LO}(s)$, (a) $l_1 : 150 \rightarrow 700$, $l_2 : 350$ (b) $l_2 : 0 \rightarrow 700$, $l_1 : 250$

of J_L $(\dot{J}_L)$ can be obtained.

$$\dot{J}_L = -\tilde{\chi}_1\left(\frac{1}{C_o}\tilde{\chi}_2 + l_1\tilde{\chi}_1\right) - l_2\tilde{\chi}_2\tilde{\chi}_1 < 0 \tag{22}$$

Another way to analyze stability is by observing the Nyquist plot. The open-loop transfer function of the proposed notch filter-based current observer can be derived from Fig. 5(b)

$$G_o(s) = \frac{l_2}{C_o(s + l_1)} g_n(s) \tag{23}$$

The Nyquist plot of G_o has been shown in Fig. 9 for different values of observer gain and ζ. It can be seen that the curve is always away from the critical point (-1,0). In Fig. 9(a) the Nyquist plot for different values of l_1 and l_2 has been shown separately. It can be seen that the gain values of the observer greatly affect the stability, as said in the previous section. Higher values of l_1 imply close proximity to the critical point, whereas larger values of l_2 signify that the curve will be far away from the critical point, which ensures stability. Furthermore, the values of the damping factor of the notch filter ζ are also varied to study the effect on stability. It can be seen from Fig. 9(b) that it has a limited impact on stability. A small value of ζ will make the system underdamped.

2) Tracking Performance Analysis of the Observer: The tracking performance of the current observer loop for both cases can be analyzed from the bode plot of the close loop transfer function $G_e{}^{LO}(s)$ and $G_e^{NF-LO}(s)$. Reflects the dynamic response of the current loop. In Fig. 10 (a) the bode plot with different observer gains has been plotted. It can be seen that the controller successfully tracks the reference in the range of 2500 rad/sec with l_1=350. A higher value of l_2

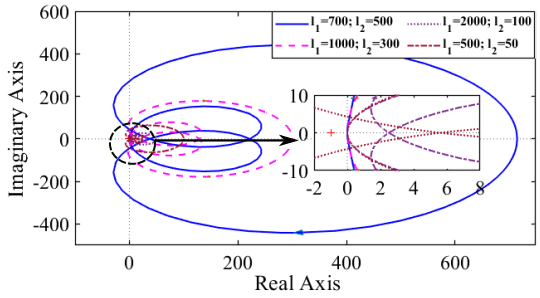

(a)

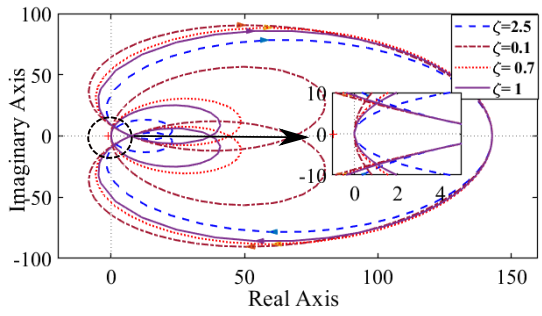

(b)

Fig. 9. Nyquist plot of $G_o(s)$ for (a) different observer gain (b) different damping ratio ζ

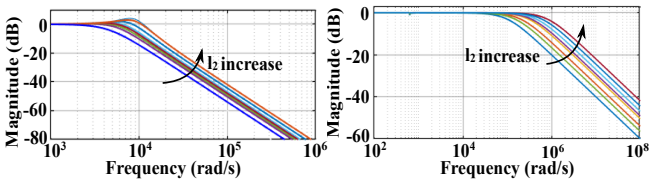

(a) (b)

Fig. 10. Bode plot of (a) ${G_e}^{LO}(s)$ (b) $G_e^{NF-LO}(s)$ when l_2 is increasing

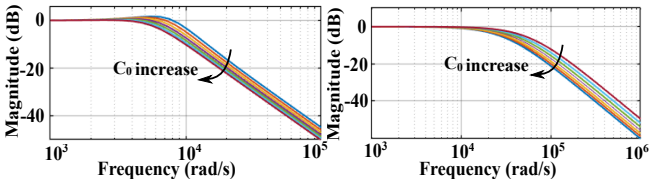

(a) (b)

Fig. 11. Bode plot of (a) ${G_e}^{LO}(s)$ (b) $G_e^{NF-LO}(s)$ for varying C_0

shows a higher overshoot, and a lower value of l_2 shows a faster deviation from 0 dB. This implies a slower response.

In Fig. 10(b), the observer with a notch filter shows better tracking performance. It shows a deviation from 0 dB in the higher frequency range. In this case, the lower values of l_2 cause a deviation in the lower frequency range, keeping l_1 fixed at 350.

3) Robustness Analysis of the Observer: The robustness of the observer has been studied with parametric variation. From ${G_e}^{LO}(s)$ and $G_e^{NF-LO}(s)$ it is evident that the observer's response depends on the circuit parameter C_o. Here, the variation in capacitance $\pm 30\%$ has been considered. The Bode plot of the closed-loop transfer function of the current observer loop is shown in Figs. 11(a) and 11(b). It can be understood that the deviation of the capacitance from the theoretical value does not cause system instability, but rather affects the system response. A lower capacitance value causes an overshoot in the transient response, whereas tracking ability slightly decreases with increased capacitance.

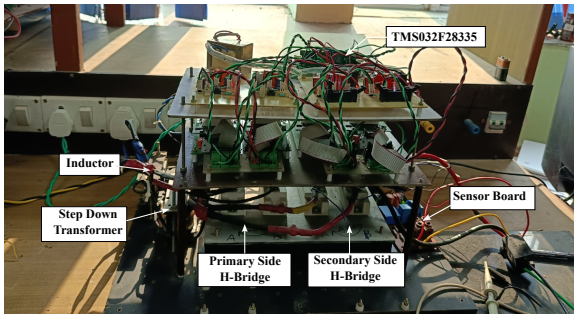

Fig. 12. Hardware setup of DAB converter

TABLE I
DAB CONVERTER PARAMETERS.

Parameter	Value
Input Voltage (V_i), Output Voltage (V_o)	200 V & 50 V
Output Power (P_o), Switching Frequency (f_{sw})	750 W, 10 kHz
Turns Ratio (n)	4:1
Leakage Inductance (L_p), Output Capacitance (C_o)	165 μH,1000 μF
HV side IGBT module	SKM75GB063D
LV side IGBT module	SKM145GB066D
SMC Parameter: κ_1 and κ_2	0.023 and 8.67
Observer gain: l_1 and l_2	700 and 380
Notch Filter Parameter: ζ and g_{min}	0.7 and 0.5

IV. EXPERIMENTAL RESULT

To confirm the practical efficacy and performance of the proposed controller, an experimental framework was established. Fig. 12 presents the experimental setup of the DAB converter, while Table I meticulously outlines the converter's detailed specifications. For precise monitoring and evaluation of the output voltage, an isolated voltage sensor, the LV25p, was used. The measured analog signal was then accurately quantified by the 12-bit analog-to-digital converter integrated within the TMS320F28335 digital signal processor (DSP). Control algorithms were designed and executed within the MATLAB computational environment in the discrete-time domain, with a fixed sampling rate of 10 μs to accurately capture the dynamics of the DAB converter. The output of the control algorithms is fed to the on-chip digital enhanced pulse width modulator (ePWM), which generates the switching signals for the primary and secondary bridges of the DAB converter. To thoroughly test and substantiate the proposed control system, a series of test scenarios were conducted, including:

1) Scenario 1: The dynamic response of the system to load variations of ±50% was tested to gain insight into the controller's adaptability to sudden load changes.

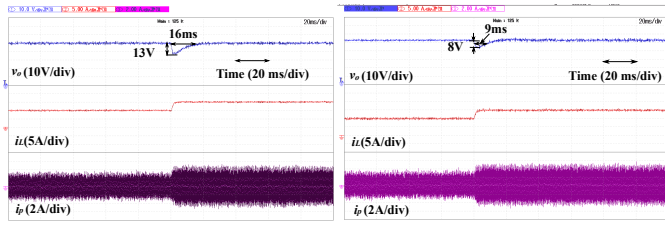

(a) (b)

Fig. 13. Transient response of the DAB converter when i_L is increased by 50% under (a) SM controller [18] (b) LO-SM controller.

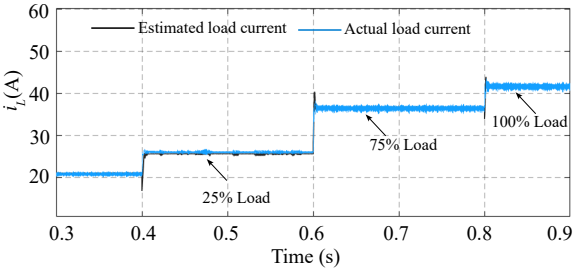

Fig. 15. Response of the estimated current and actual load current when the load is varying

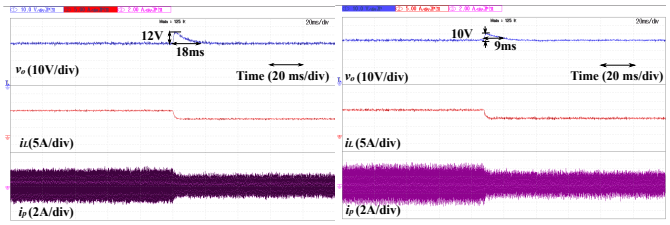

(a) (b)

Fig. 14. Transient response of the DAB converter when i_L is decreased by 50% under (a) SM controller [18] (b) LO-SM controller.

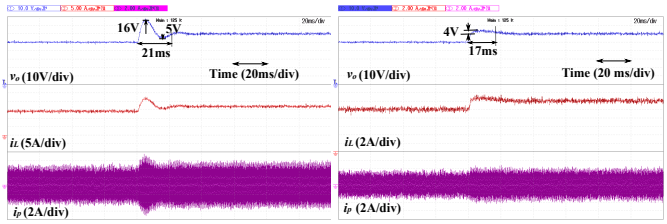

(a) (b)

Fig. 16. Transient response of DAB converter: V_o^* is step changed from 50 V to 60 V under (a) SM controller [18] (b) LO-SM controller.

2) Scenario 2: The system's ability to follow changes in the output reference voltage was analyzed, assessing the precision of the control mechanism's tracking ability.
3) Scenario 3: The performance implications of different observer gains were studied to identify optimal gains for accurate state estimation.
4) Scenario 4: A robustness assessment was performed by subjecting the system to various parameter changes to evaluate the controller's stability and reliability under diverse operating conditions.
5) Scenario 5: The system's capability to maintain performance in a cascaded architectural environment was evaluated.

These scenarios were carefully selected to cover a broad range of operational conditions, ensuring a thorough scrutiny and validation of the controller's effectiveness.

A. Scenario 1

In this test scenario, a stable 200 V DC voltage source provides the input voltage to the converter. The experiment involves an abrupt change in the resistive load, causing the current to initially surge from 10 A to 15 A and subsequently drop from 15 A to 10 A. The dynamic behavior of the proposed LO-SMC [P] control strategy is evaluated against sliding mode control (SMC) [18] technique with the inclusion of a current sensor.

Figs. 13 and 14 provide a comparative analysis of the two controllers during the load step changes (ΔI_L). Fig. 13 illustrates the system's performance with an increased load from 10 A to 15 A, while Fig. 14 captures the transient performance when the load current is reduced from 15A to 10A. These figures demonstrate the output voltage, output current, and inductor current waveforms with different divisions indicated for clarity: 10V/div for the output voltage, and 5A/div and 2A/div for the output and inductor currents, respectively. In Figs. 13(a) and 14(a), the SM controller's transient response is displayed. This response reveals a settling time (t_{sm}) of the output voltage is 16 ms with a 13 V undershoot (V_o^m) upon load increase, and 18 ms settling time with 12 V overshoot (V_o^m) when the load is decreased. Contrastingly, the implementation of the LO-SMC approach, shown in Figs. 13(b) and 14(b). This approach refines the dynamic response for both load changes by eliminating the need for a sensor and bypassing the additional phase lag induced by filters in the current loop, which otherwise slows the response. With the LO-SMC, the voltage undershoot is reduced to 8 V, and the settling time is reduced to 9 ms when the load increases. A consistent improvement is observed with load decrease; the voltage overshoot is curtailed to 10 V, and the system settles in just 9 ms. These results underscore the superiority of sensorless control strategies in enhancing system responsiveness. Moreover, the simuation results of the estimated current and actual current has been shown in Fig. 15 where the load current ranges from 25% to 75% and from 75% to 100% at t = 0.4 s, 0.6 s, 0.8 s. It can be seen that the estimated load current can successfully track the actual load current for different load.

B. Scenario 2

In the evaluation of the controller's tracking performance to follow a set reference, the second test scenario introduces a change in the reference output voltage (ΔV_o^*), increasing it by 10 volts. This test is critical for observing how effectively the controller can match its output to a changing target voltage. Fig. 16 (a) captures the behavior of the SM controller under these conditions. The waveform indicates a pronounced peak of 16 V above the desired voltage (overshoot) followed by an undershoot of 5 V, signifying considerable deviation

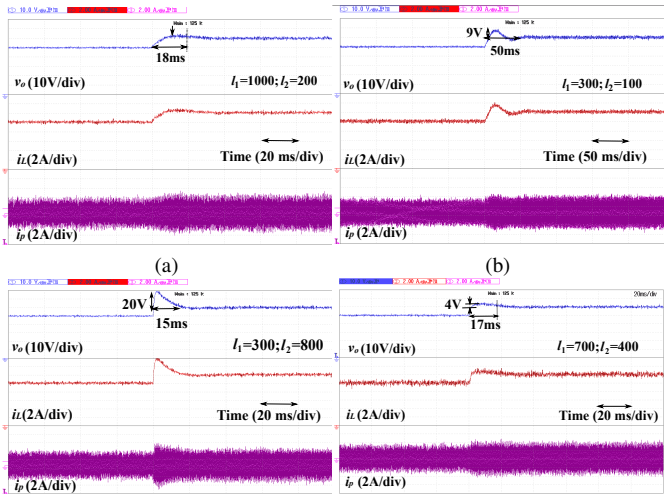

Fig. 17. Transient response when $\Delta V_o^* \rightarrow\uparrow$10 V (50 V to 60 V) under LO-SMC for different values of observer gain

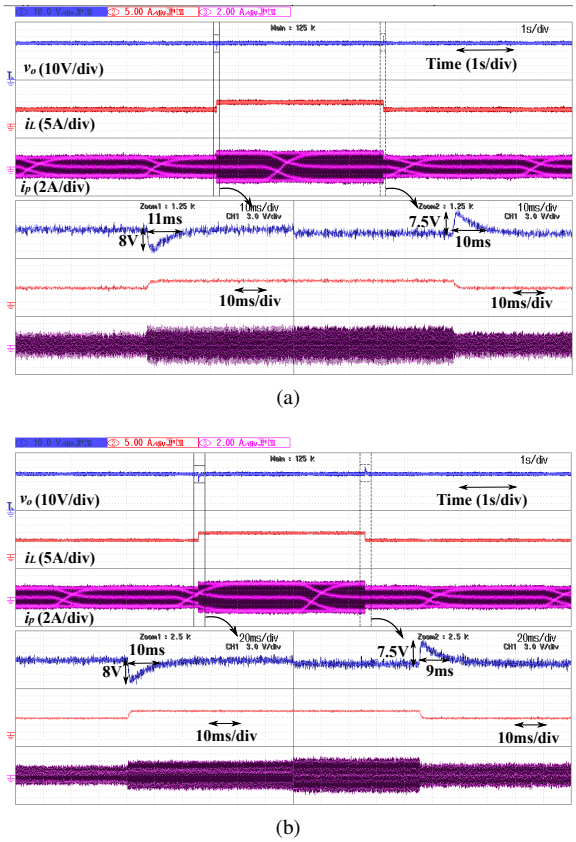

Fig. 18. Transient response of DAB converter when load is varying $\pm 50\%$ under leakage inductance variation (a) -20% (b) $+20\%$

from the intended outcome. Additionally, the trace denotes a considerable delay to the track set reference, with the settling time reaching 21 ms. Moving to the proposed LO-SMC, as represented in Fig. 16(b), a clear improvement in performance is discerned. This controller registers an impressive improvement with a minimal overshoot of merely 4 V. Moreover, the controller achieves a settling time of only 17 ms, marking a

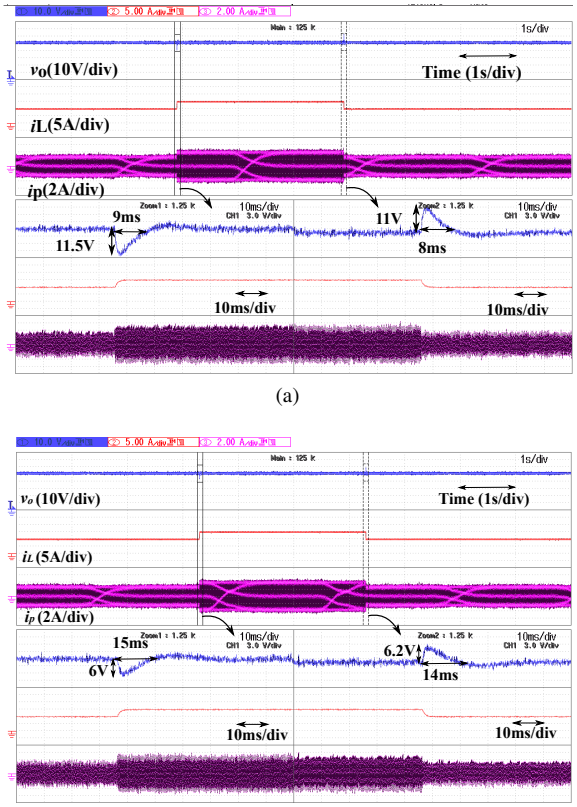

Fig. 19. Transient response of DAB converter when load is varying $\pm 50\%$ under output capacitance variation (a) -20% (b) $+20\%$

significant advancement in tracking precision. This outcome illustrates a substantial enhancement in the controller's ability to swiftly and accurately align the output voltage with a newly set reference, underscoring its superior dynamic performance.

C. Scenario 3

The third test scenario was executed to scrutinize the dynamic response of the system under varying observer gain settings. Theoretical studies had previously indicated that lower values of observer gain l_1 tend to extend the settling time, while excessively high gains can push the system into an overdamped state. On the contrary, higher vales of l_2 may achieve faster convergence, although at the expense of increased overshoot. This behavior was also confirmed during practical experiments. A step change in the reference voltage from 50V to 60V was introduced to observe the system's transient response. In Fig. 17(a), the output voltage, the output current, and the inductor current are displayed for an observer gain setting where l_1 is set to 1000 and l_2 to 200. This particular selection of l_1 exceeds its optimal value, resulting in an overdamped response to voltage steps. The system response displays a settling time of 18 ms without any overshoot in voltage, characteristic of an overdamped system. Fig. 17(b) reveals the system's transient behavior with both observer gains set to lower values, specifically l_1 at 300 and l_2 at 100. Such lower values significantly decelerate the system response.

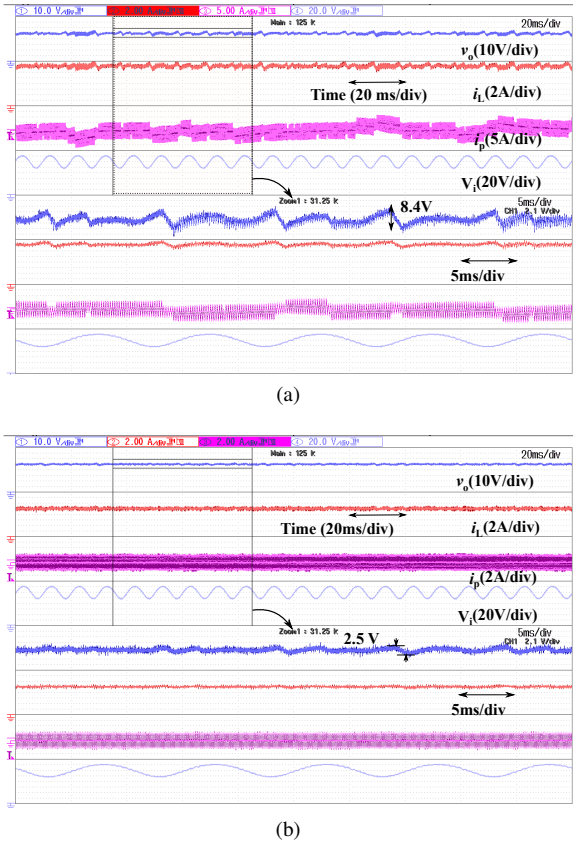

Fig. 20. Steady state waveform of DAB converter when cascaded with single phase AC/DC converter under (a) SMC [18] (b) proposed LO-SMC

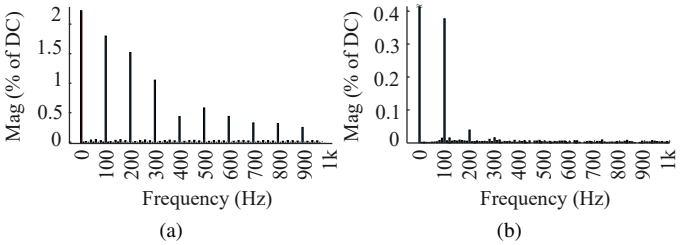

Fig. 21. FFT spectrum of v_o under (a) SMC [18] (b) proposed LO-SMC.

The result is a sluggish response with a settling time of 50 ms and a voltage overshoot of approximately 9 V. Proceeding to a configuration where l_2 increases beyond its optimal value, as illustrated in Fig. 17(c), the system exhibits behavior consistent with theoretical predictions. The higher overshoot of 20 volts is observed with a reduced t_{sm} of 15 ms, which indicates a quicker but less stable response. On the contrary, Fig. 17(d) delineates the transient response when both l_1 and l_2 are tuned to their optimal values, here 700 for l_1 and 400 for l_2. This judicious selection of observer gains strikes a balance between response time and overshoot, yielding a more desirable dynamic behavior. The voltage overshoot is contained at 4 V and t_{sm} is 16 ms. The resulting waveform of the output voltage following the applied disturbance exhibits an optimal dynamic response, as it manages to minimize overshoot with lesser settling time.

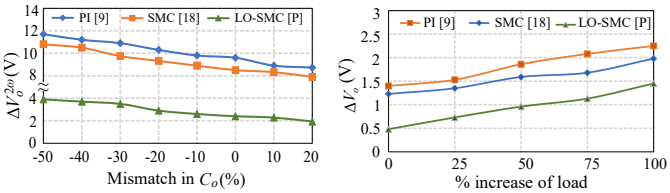

Fig. 22. Performance comparison (a) $\Delta V_o^{2\omega}$ during C_o mismatch (b) ΔV_o under varying loads

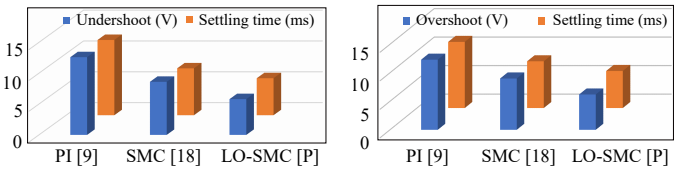

Fig. 23. V_o^m and t_{sm} during input voltage (a) decrease by 25% (b) increase by 25%

D. Scenario 4

The robustness of the system against variations in circuit parameters was tested in the fourth scenario. This scenario focused on evaluating the effects of deviation in two specific parameters: leakage inductance and output capacitance, which varied within a defined range. To measure the impact of these parameter mismatches, the load current was initially increased from 10 A to 15 A and subsequently decreased back to 10 A. This allowed for a thorough examination of the transient response under conditions of parameter variation. It is important to recognize that deviations in the leakage inductance value do not significantly alter the transient or steady-state performance of the controller because any mismatch in inductance only modifies the operating phase shift ratio without affecting overall system performance. In Fig. 18, the waveforms for the output voltage, output current, and inductor current are presented. The two transient instances, where the load current is increased and then decreased, are highlighted within two inset boxes marked by black arrows. Fig. 18(a) shows the behavior of the system with a 20% reduction in the inductance value, while Fig. 18(b) illustrates the response to a 20% increase in inductance. In both instances, it is evident that the voltage overshoot and the settling time remain relatively unchanged. The overshoot lies between 7.5 V to 8 V, and the settling time varies from 9 to 11 ms, figures that align closely with those obtained when the theoretical inductance matches the actual value. Hence, it can be concluded that the inductance mismatch does not significantly impair the performance of the controller.

The situation differs, however, when discrepancies in output capacitance are considered. The transient response is greatly influenced by the capacitance value. In Fig. 19(a), the system's transient behavior is depicted when the capacitance is decreased by 20%. A zoomed-in view at both instances of load change, indicated by black arrows, shows that a reduced capacitance value leads to a higher voltage over-

TABLE II
COMPARATIVE ANALYSIS UNDER VARIOUS TEST CONDITIONS

		PI [9]	SMC [18]	LO-SMC [P]
ΔI_L: 10→15 A	V_o^m	-16	-13	-8
	t_{sm} (ms)	22	12	9
ΔI_L: 15→10 A	V_o^m	18	11	10
	t_{sm} (ms)	25	10	9
ΔV_o^* →↑10 V	V_o^m	20	16	4
	t_{sm} (ms)	34	21	17
ΔV_i: 200→150 V	V_o^m	-11.6	-8.2	-6.5
	t_{sm} (ms)	12.3	9	6.2
ΔV_i: 200→250 V	V_o^m	12.2	7.6	6
	t_{sm} (ms)	12.6	8.6	5.8
Cascaded topology	$\Delta V_o^{2\omega}$	9.6	8.4	2.5
	% of 2ω ripple	-	1.7	0.38

shoot—approximately 12 V, which is notably higher compared to scenarios where the theoretical and practical capacitance values are equal. However, settling time remains relatively consistent. Conversely, Fig. 19(b) presents the outcome when the capacitance is increased by 20%. Here, the voltage overshoot is substantially diminished, but at the expense of a more sluggish system response. The overshoot drops to around 6 V, while the settling time extends to 15 ms. This observation is in complete harmony with theoretical predictions, illustrating that an increase in capacitance typically results in a more damped response, thereby reducing overshoot but also slowing down the transient recovery.

E. Scenario 5

In this scenario, the DAB converter is integrated with a fully controlled single-phase AC/DC converter, providing a DC link input voltage of 200 V. This section conducts a comparative analysis of the DAB converter's performance under the control of a SMC [18] and the proposed LO-SMC [P]. The steady-state waveforms for both control scenarios are depicted in Figs. 20(a) and 20(b). Across these illustrations, the topmost waveform represents the output voltage of the DAB converter, followed by the output current, the leakage inductor current, and finally, the bottom trace displaying the input DC link voltage supplied to the DAB converter. Fig. 20(a) illustrates the performance with SM controller, revealing notable double-line frequency ripple in both the output voltage and current of the DAB converter. A closer inspection of the waveforms exposes that the voltage ripple ($\Delta V_o^{2\omega}$) 8.4 V, constituting nearly 16% of the output voltage. This level of ripple can potentially impact the battery's operational lifespan. Conversely, the implementation of the proposed LO-SMC effectively mitigates the double-line frequency ripple, accomplishing this without the need for additional hardware, as illustrated in Fig. 20(b). Zooming in on the voltage traces in Fig. 20(b) the ripple ($\Delta V_o^{2\omega}$) significantly reduced and it is mere 5% of the output voltage. To visually represent the reduction in double-line frequency ripple in the output voltage, Fast Fourier Transform (FFT) analysis of the DC-Bus voltage was performed. Figs. 21(a) and 21(b) showcase the FFT analyses of the DC bus voltage under SM control and the proposed control, respectively. These graphs were generated from MATLAB-based simulation results. Comparing both bar graphs demonstrates the significant effectiveness of the proposed controller in suppressing double-line frequency ripple. Furthermore, the suppression of other harmonics, as evident in Fig. 21(b), serves as compelling evidence of the proposed controller's success in enhancing system performance.

F. Comparative Performance

Table II presents a detailed comparison of three control methods—proportional-integral (PI) based feedback linearized control method [9], SMC, and proposed LO-SMC—applied to a DAB converter under different test conditions. The PI controller has been fine-tuned to achieve a crossover frequency of 1.5 kHz with a phase margin of 45 degrees to ensure system stability and responsiveness. This section quantifies performance in terms of voltage overshoot/undershoot and settling time, crucial metrics for evaluating control quality. For load increases from 10 A to 15 A, the LO-SMC outperforms the others with the least voltage deviation and fastest settling. When the load decreases from 15 A to 10 A, the differences are less pronounced, but LO-SMC still leads with minimal overshoot and quick settling. Notably, the reference voltage increment test highlights LO-SMC's superior precision, showing only a 4V overshoot. Finally, when integrated with an AC/DC converter, the proposed LO-SMC significantly reduces output voltage ripple and harmonic distortion, demonstrating its effectiveness in creating a stable and efficient system. Additionally, Fig. 22(a) illustrates the double line frequency ripple, for three different controllers operating under capacitance mismatch. This comparison reveals that the voltage ripples for both PI and SM controllers are considerably larger than those for the proposed controller. Fig. 22(b) displays the output voltage ripple (ΔV_o) variations for the three controllers when the load is increased incrementally by 25%, 50%, 75%, and 100%. In these tests as well, the proposed controller demonstrates a smaller voltage ripple compared to the traditional ones. Fig. 23 features a bar chart that compares the controllers' performance in response to changes in input voltage (ΔV_i), focusing on convergence time and voltage overshoot / undershoot. Across these parameters, the proposed controller consistently exhibits better performance.

V. CONCLUSION

Key challenges in DAB converters, including slow response to load changes and double-line frequency ripple in single-phase AC/DC configurations, have been successfully addressed in this work. A LO-SMC is proposed, eliminating the need for current sensors and demonstrating superior dynamic performance even under significant load variations (±50%). To combat ripple, a notch filter has been integrated into the current observer loop without compromising system stability. The ripple in the control law is demonstrably reduced by this filter, and the designed observer effectively tracks the load current across different load conditions. The proposed control method has been shown to outperform traditional PI and SM controllers in various tests, demonstrating its advantages. The robustness and effectiveness of our control strategy and parameter design have been confirmed by real-time hardware

validation. Integration of DPS or EPS modulation techniques could be explored in future research for even stricter performance demands or dynamic operating conditions. Additional potential enhancements include extending the observer to handle more sensor input and investigating adaptive gain strategies for highly dynamic loads.

REFERENCES

[1] P. Pal and R. K. Behera, "Observer based current sensorless control for dab converter with improved dynamic performance," in *2022 IEEE International Conference on Power Electronics, Drives and Energy Systems (PEDES)*, 2022, pp. 1–6.

[2] L. Li, K.-J. Li, K. Sun, and Z. Liu, "A three-port psfb/dab-mmc pet with inertia enhancement under lvdc disturbance," *IEEE Transactions on Industry Applications*, vol. 59, no. 1, pp. 300–311, Jan.-Feb. 2023.

[3] J. Lu, K. Bai, A. R. Taylor, G. Liu, A. Brown, P. M. Johnson, and M. McAmmond, "A modular-designed three-phase high-efficiency high-power-density ev battery charger using dual/triple-phase-shift control," *IEEE Transactions on Power Electronics*, vol. 33, no. 9, pp. 8091–8100, Sept. 2018.

[4] J. A. Mueller and J. W. Kimball, "An improved generalized average model of dc–dc dual active bridge converters," *IEEE Transactions on Power Electronics*, vol. 33, no. 11, pp. 9975–9988, Nov. 2018.

[5] M. T. Iqbal and A. I. Maswood, "An explicit discrete-time large- and small-signal modeling of the dual active bridge dc–dc converter based on the time scale methodology," *IEEE Journal of Emerging and Selected Topics in Industrial Electronics*, vol. 2, no. 4, pp. 545–555, Oct. 2021.

[6] K. Zhang, Z. Shan, and J. Jatskevich, "Large- and small-signal average-value modeling of dual-active-bridge dc–dc converter considering power losses," *IEEE Transactions on Power Electronics*, vol. 32, no. 3, pp. 1964–1974, March 2017.

[7] H. Qin and J. W. Kimball, "Closed-loop control of dc–dc dual-active-bridge converters driving single-phase inverters," *IEEE Transactions on Power Electronics*, vol. 29, no. 2, pp. 1006–1017, Feb. 2014.

[8] H. Y. Kanaan, M. Caron, and K. Al-Haddad, "Design and implementation of a two-stage grid-connected high efficiency power load emulator," *IEEE Transactions on Power Electronics*, vol. 29, no. 8, pp. 3997–4006, 2014.

[9] A. Tong, L. Hang, H. S.-H. Chung, and G. Li, "Using sampled-data modeling method to derive equivalent circuit and linearized control method for dual-active-bridge converter," *IEEE Journal of Emerging and Selected Topics in Power Electronics*, vol. 9, no. 2, pp. 1361–1374, April 2021.

[10] D. Segaran, D. G. Holmes, and B. P. McGrath, "Enhanced load step response for a bidirectional dc–dc converter," *IEEE Transactions on Power Electronics*, vol. 28, no. 1, pp. 371–379, Jan. 2013.

[11] W. Zhao, X. Zhang, S. Gao, and M. Ma, "Improved model-based phase-shift control for fast dynamic response of dual-active-bridge dc/dc converters," *IEEE Journal of Emerging and Selected Topics in Power Electronics*, vol. 9, no. 1, pp. 223–231, Feb. 2021.

[12] W. Song, N. Hou, and M. Wu, "Virtual direct power control scheme of dual active bridge dc–dc converters for fast dynamic response," *IEEE Transactions on Power Electronics*, vol. 33, no. 2, pp. 1750–1759, Feb. 2018.

[13] K. Li, Y. Yang, S.-C. Tan, and R. S.-Y. Hui, "Sliding-mode-based direct power control of dual-active-bridge dc-dc converters," in *2019 IEEE Applied Power Electronics Conference and Exposition (APEC)*, 2019, pp. 188–192.

[14] Q. Xiao, L. Chen, H. Jia, P. W. Wheeler, and T. Dragičević, "Model predictive control for dual active bridge in naval dc microgrids supplying pulsed power loads featuring fast transition and online transformer current minimization," *IEEE Transactions on Industrial Electronics*, vol. 67, no. 6, pp. 5197–5203, June 2020.

[15] S. Dutta, S. Hazra, and S. Bhattacharya, "A digital predictive current-mode controller for a single-phase high-frequency transformer-isolated dual-active bridge dc-to-dc converter," *IEEE Transactions on Industrial Electronics*, vol. 63, no. 9, pp. 5943–5952, Sept. 2016.

[16] B. Liu, Y. Zha, T. Zhang, and S. Chen, "Fuzzy logic control of dual active bridge in solid state transformer applications," in *2016 Tsinghua University-IET Electrical Engineering Academic Forum*, 2016, pp. 1–4.

[17] Y.-C. Jeung and D.-C. Lee, "Voltage and current regulations of bidirectional isolated dual-active-bridge dc–dc converters based on a double-integral sliding mode control," *IEEE Transactions on Power Electronics*, vol. 34, no. 7, pp. 6937–6946, July 2019.

[18] N. Tiwary, V. Naik N, A. K. Panda, A. Narendra, and R. K. Lenka, "A robust voltage control of dab converter with super-twisting sliding mode approach," *IEEE Journal of Emerging and Selected Topics in Industrial Electronics*, vol. 4, no. 1, pp. 288–298, Jan. 2023.

[19] J. Ge, Z. Zhao, L. Yuan, and T. Lu, "Energy feed-forward and direct feed-forward control for solid-state transformer," *IEEE Transactions on Power Electronics*, vol. 30, no. 8, pp. 4042–4047, Aug. 2015.

[20] F. Xiong, J. Wu, Z. Liu, and L. Hao, "Current sensorless control for dual active bridge dc–dc converter with estimated load-current feedforward," *IEEE Transactions on Power Electronics*, vol. 33, no. 4, pp. 3552–3566, April 2018.

[21] W. Zhang, D. Xu, P. N. Enjeti, H. Li, J. T. Hawke, and H. S. Krishnamoorthy, "Survey on fault-tolerant techniques for power electronic converters," *IEEE Transactions on Power Electronics*, vol. 29, no. 12, pp. 6319–6331, Dec. 2014.

[22] L. Zhang and G.-H. Yang, "Observer-based adaptive decentralized fault-tolerant control of nonlinear large-scale systems with sensor and actuator faults," *IEEE Transactions on Industrial Electronics*, vol. 66, no. 10, pp. 8019–8029, Oct. 2019.

[23] S. K. Kommuri, J. J. Rath, and K. C. Veluvolu, "Sliding-mode-based observer–controller structure for fault-resilient control in dc servomotors," *IEEE Transactions on Industrial Electronics*, vol. 65, no. 1, pp. 918–929, Jan. 2018.

[24] X. Liu, M. Zhang, Y. Wang, and E. Rogers, "Design and experimental validation of an adaptive sliding mode observer-based fault-tolerant control for underwater vehicles," *IEEE Transactions on Control Systems Technology*, vol. 27, no. 6, pp. 2655–2662, Nov. 2019.

[25] G. Wang, X. Hao, N. Zhao, G. Zhang, and D. Xu, "Current sensor fault-tolerant control strategy for encoderless pmsm drives based on single sliding mode observer," *IEEE Transactions on Transportation Electrification*, vol. 6, no. 2, pp. 679–689, June 2020.

[26] M. Zolfaghari, G. B. Gharehpetian, and A. Anvari-Moghaddam, "Quasi-luenberger observer-based robust dc link control of uipc for flexible power exchange control in hybrid microgrids," *IEEE Systems Journal*, vol. 15, no. 2, pp. 2845–2854, June 2021.

[27] V. K. Dunna, K. P. B. Chandra, P. K. Rout, and B. K. Sahu, "Design and real-time validation of higher order sliding mode observer-based integral sliding mode mppt control for a dc microgrid," *IEEE Canadian Journal of Electrical and Computer Engineering*, vol. 45, no. 4, pp. 418–425, Fall 2022.

[28] Y. Gui, F. Blaabjerg, X. Wang, J. D. Bendtsen, D. Yang, and J. Stoustrup, "Improved dc-link voltage regulation strategy for grid-connected converters," *IEEE Transactions on Industrial Electronics*, vol. 68, no. 6, pp. 4977–4987, June 2021.

[29] D. Çelik, H. Ahmed, and M. E. Meral, "Kalman filter-based super-twisting sliding mode control of shunt active power filter for electric vehicle charging station applications," *IEEE Transactions on Power Delivery*, vol. 38, no. 2, pp. 1097–1107, April 2023.

[30] Y. Zhang, J. Fang, F. Gao, T. Song, S. Gao, and D. J. Rogers, "Second-harmonic ripple voltage suppression of integrated single-phase pulsewidth modulation rectifier charging system for evs," *IEEE Transactions on Power Electronics*, vol. 35, no. 4, pp. 3616–3626, April 2020.

[31] L. Cao, K. H. Loo, and Y. M. Lai, "Output-impedance shaping of bidirectional dab dc–dc converter using double-proportional-integral feedback for near-ripple-free dc bus voltage regulation in renewable energy systems," *IEEE Transactions on Power Electronics*, vol. 31, no. 3, pp. 2187–2199, March 2016.

[32] M. Ali, M. Yaqoob, L. Cao, and K. H. Loo, "Disturbance-observer-based dc-bus voltage control for ripple mitigation and improved dynamic response in two-stage single-phase inverter system," *IEEE Transactions on Industrial Electronics*, vol. 66, no. 9, pp. 6836–6845, Sept. 2019.

[33] J. You, D. M. Vilathgamuwa, N. Ghasemi, and W. L. Malan, "An active power decoupling method for single phase dc/ac dab converters," *IEEE Access*, vol. 7, pp. 12 964–12 972, 2019.

Piyali Pal (Graduate Student Member, IEEE) received her B.Tech and M.Tech degree in electrical engineering from University of Calcutta, Kolkata, India, in 2018 and 2020, respectively. She is currently pursuing her Ph.D. in Electrical Engineering at the Indian Institute of Technology, Patna, India. Her research interests include the design of the EV charger, DC microgrid, control of the bidirectional DC-DC converter, and its sensorless and fault-tolerant control approach.

Ranjan Kumar Behera (Senior Member, IEEE) received the B.Eng. degree in electrical engineering from the Regional Engineering College Rourkela, Rourkela, India, in 1998, and the M.Tech. and Ph.D. degrees in electrical engineering from the Indian Institute of Technology Kanpur, Kanpur, India, in 2003 and 2009, respectively. Since 2009, he has been a Faculty Member and is currently an Associate Professor with the Department of Electrical Engineering, Indian Institute of Technology Patna, Patna, India. His research interests include applications of non-linear control theory to power electronic converters, pulse width modulation techniques, and multiphase electric drive control.
Dr. Behera was the recipient of the 2022 IEEE Outstanding Paper Award for the IEEE Transactions on Industrial Electronics.

Utkal Ranjan Muduli (Senior Member, IEEE) received the B.Tech. degree in electrical and electronics engineering from the Biju Patnaik University of Technology, Rourkela, India, in 2011, the M.Tech. degree in electrical engineering from the Indian Institute of Technology Gandhinagar, India, in 2014, and a Ph.D. degree in electrical engineering from the Indian Institute of Technology Patna, India, in 2022. He was a visiting scholar and research associate with the Department of Electrical Engineering and Computer Science, Khalifa University, Abu Dhabi, UAE, in 2019 and 2021, respectively, where he is currently a postdoctoral research fellow. His research interests include modulation strategies for multiphase motor drives, matrix converters and their control, battery power management, and wireless power transfer. Dr. Muduli was the recipient of the 2022 IEEE Outstanding Paper Award for IEEE Transactions on Industrial Electronics.